Tuning Perovskites' Hydration-Induced Chemical Expansion with Octahedral Tilt Angles

Lawrence O. Anderson^{1,2}, Qiang Zhang³, and Nicola H. Perry^{1,2*}

- 1. Department of Materials Science and Engineering, University of Illinois Urbana-Champaign, 1304 W Green St., Urbana, IL, 61801 U.S.A.
- 2. Materials Research Laboratory, University of Illinois Urbana-Champaign, 104 S. Goodwin Ave., Urbana IL, 61801, U.S.A.
- 3. Neutron Science Division, Oak Ridge National Laboratory, Oak Ridge, Tennessee 37831, USA
- * Corresponding author. Email: nhperry@illinois.edu

Abstract

Hydration-induced strains in proton-conducting oxides compromise chemo-mechanical stability when these materials are applied in protonic ceramic electrochemical cells. To develop design principles for zero-strain materials, we systematically studied the hydration coefficients of chemical expansion (CCEs) in perovskite (Sr,Ba)(Ce,Zr,Y)O_{3-x} solid solutions with in-situ dilatometry and thermogravimetric analysis in the range 430-630 °C. By including and decoupling a wide range of tolerance factors and lattice parameters, we were able to identify a minimum in hydration CCEs (0-0.02) at intermediate tolerance factor values ($t\approx0.95$). Conversely, despite expectations of lower CCEs in larger unit cells, no general trend in CCE vs. lattice parameter was found, and opposite trends could be seen for Sr(Ce,Zr,Y)O_{3-x} vs. Ba(Ce,Zr,Y)O_{3-x} separately. *In*situ neutron diffraction enabled atomistic insight. With decreasing t, chemical strain anisotropy increased, but this trend did not match the U-shaped dependence of macroscopic CCEs on t. Instead, perovskites with intermediate t, hosting intermediate octahedral tilt angles in the nominally dry state, underwent the largest change in B-O-B angles during hydration. Accommodating hydration through decreasing B-O-B angles is beneficial because it does not result in large lattice parameter changes. We propose intermediate tolerance factor as a simple structural descriptor to enable near-zero hydration strains in proton-conducting perovskites.

1. Introduction

Intermediate-temperature (400-600 °C) electrochemical cells provide a compelling alternative to high-temperature (600-1000 °C) solid oxide fuel/electrolysis cells (SOFC/SOEC) and low-temperature (25-100 °C) PEM cells. In the intermediate-temperature range, proton conductivities in select oxides can exceed the oxide-ion conductivity of common SOFC/SOEC electrolytes[1], [2], like yttria-stabilized zirconia (YSZ)[3]; therefore, proton-conducting ceramic electrolytes are enabling materials for these lower temperature cells with potential for lower cost interconnects and the use of waste heat. Protonic ceramic electrolysis cells (PCECs) offer the added benefit (over SOECs) of producing H₂ that is free from H₂O, so further processing to remove the steam is unnecessary. The ability of a perovskite composition to hydrate benefits from oxideion basicity, with compositions containing electropositive Ba or Sr A-site cations receiving significant attention (particularly those with Ba)[4], [5], [6], [7], [8], [9], [10], [11]. Kreuer et al[1] have also suggested that similar electronegativities between A- and B-site cations result in the most negative hydration enthalpies, which is supported by the extensive use of Ce and Zr as B-site cations in proton conducting electrolytes[5], [6], [7], [9], [10], [12], [13], [14], [15], [16], [17]. Zirconate compositions can offer high ionic conductivity and stability, but sintering challenges can lead to high grain boundary electrical resistance[18], [19], [20]. Cerate compositions densify at lower temperatures, but they suffer from a low tolerance for humid, CO₂ containing environments, and their higher n-type electronic conductivity under reducing conditions is less suitable for monolithic electrolyte applications[21], [22]. Intermediate compositions, or the inclusion of other A and/or B-site cations with desirable processing or performance characteristics can offer a compromise of material properties for efficient and stable devices.

The importance of selecting materials for device components based on properties like ionic conductivity, electronic conductivity, and thermodynamic stability in steam and with respect to neighboring materials should not be understated, but there has also been growing interest in understanding a material's chemo-mechanical response, i.e., chemical expansivity, to improve the stability and longevity of operation[4], [5], [6], [23]. As stoichiometry changes via insertion/removal of ions from/to the gas phase, there is a corresponding mechanical strain that, in multilayer devices, can result in warping, delamination, and/or fracture. For proton-conducting oxides with significant oxygen vacancy concentrations and low electronic carrier populations, which are desirable traits for electrolytes, the hydration reaction is of primary interest:

$$v_0^{\bullet\bullet} + 0_0^{\times} + H_2 0 \leftrightarrow 2(0H)_0^{\bullet} \tag{1}$$

Here, steam from the surrounding gas environment is incorporated into the lattice as H_2O splits, an oxygen vacancy $(v_0^{\bullet\bullet})$ is filled with a hydroxide ion $((OH)_0^{\bullet})$, and the remaining hydrogen effectively shares the anion site with the oxide ion (O_0^{\times}) ; therefore, the product of the hydration reaction is two hydroxide ions. From this atomistic perspective, one may consider the resulting lattice dilation in terms of the relative sizes of the "reactant" and "product" defects: Jedvik et al.[24] suggested that $(OH)_0^{\bullet}$ defects are larger than oxygen vacancies $(v_0^{\bullet\bullet})$ but smaller than oxide ions (O_0^{\times}) . In this case, the overall strain results from competition between expansion from replacing $v_0^{\bullet\bullet}$ with $(OH)_0^{\bullet}$ vs. a smaller contraction induced by replacing O_0^{\times} with $(OH)_0^{\bullet}$. To assess the degree of expansion with changing proton stoichiometry and to enable the prediction of chemical expansion in different environments, the coefficient of chemical expansion (CCE) is used, relating the isothermal linear chemical strain (ε_C) to the change in defect concentration $(\Delta[(OH)_0^{\bullet}])$:

$$CCE = \frac{\varepsilon_C}{\Delta[(OH)_O^{\bullet}]} \tag{2}$$

Considering that the ability to hydrate to a reasonable proton concentration is desirable in an electrolyte from the standpoint of conductivity, equation 2 indicates that low chemical strains should be accomplished by minimizing the CCE. Hydration-induced lattice strains of up to 1% that have been previously observed indicate the significance of this task[6], [8]. Developing a fundamental understanding of design principles for tailored hydration CCEs is therefore an important route to improve protonic ceramic cell integrity, within a context that considers both the electrical *and* chemo-mechanical properties for performance *and* longevity.

In this work, we examine the bond architecture of the most common class of oxide proton conductors, perovskites, and its impact on the magnitude of the CCE. The Goldschmidt tolerance factor, t, is a metric that describes how well a set of ions will fit geometrically into the perovskite structure:

$$t = \frac{r_A + r_X}{\sqrt{2}(r_B + r_X)} \tag{3}$$

where the weighted average ionic radii at the A-site, B-site, and anion site of an ABO_{3- δ} perovskite composition are given by r_A , r_B , and r_X , respectively. Compositions with values of t very close to 1 tend to adopt the cubic structure. As t decreases, lower symmetry perovskite structures emerge. While the cubic phase commonly transitions to rhombohedral, tetragonal, and/or orthorhombic phases as t decreases, there are also more subtle changes within a given space group. Most notably, differences in unit cell lengths along each axis become more pronounced, and octahedral tilting increases. The Goldschmidt tolerance factor is therefore a useful predictive estimate of structural features such as octahedral tilt angles, because unlike symmetry descriptors it varies continuously through a given phase and across phase transitions.

Chen et al.[5] recently studied the prototypical proton-conducting BaCe_{0.9}Y_{0.1}O_{3-δ} -BaZr_{0.9}Y_{0.1}O_{3-δ} (BCY-BZY) solid solution, experimentally and computationally, to examine the correlation between tolerance factor, symmetry, and hydration CCE. The importance of isothermal CCE measurements was highlighted, where altering the humidity stepwise at a given temperature, to induce proton stoichiometry changes, avoids complications from stoichiometry-dependent changes in thermal expansivity. The study also emphasized the importance of measuring proton concentration changes rather than assuming full hydration vs. dehydration in humid vs. nominally dry conditions. Similarly, maintaining an intermediate oxygen partial pressure and moderate temperatures ensured hydration rather than hydrogenation (with redox) as the dominant process. In that work, the DFT calculations demonstrated that B-O-B bond angles decreased (deviated further from 180°) in the hydrated state vs. dry state for both BZY and BCY. Subtle changes to the average B-O-B bond angles may contribute to the symmetry dependence of CCE by partially accommodating hydration via lattice distortions, rather than by linear unit cell strains. Ultimately, lower experimental and simulated hydration CCEs correlated to lower tolerance factors, decreasing symmetry, increasing unit cell volume, increasing oxygen vacancy radius, decreasing bulk modulus, and inter- vs. intra-octahedral hydrogen bonding. A significant monotonic relationship between tolerance factor and CCE was observed, but similarly a reverse trend of increasing unit cell volume with decreasing CCE was present for the limited composition family measured. Given multiple overlapping correlations, a study that decouples these structural factors using a broader range of compositions is needed.

In this work, we expand the hydration CCE study to a much wider range of tolerance factors using the perovskite solid solution $SrCe_{0.9-x}Zr_xY_{0.1}O_{3-\delta}$ (x = 0, 0.45, 0.9) and a new cubic $BaZr_{0.9}Y_{0.1}O_{3-\delta}$ sample, which serves as a benchmark to confirm consistency of the present results

with the prior study. Using Shannon's ionic radii[25] in Angstroms (Sr^{2+} [XII] = 1.44, Ba^{2+} [XII] = 1.61, Ce^{4+} [VI] = 0.87, Zr^{4+} [VI] = 0.72, Y^{3+} [VI] = 0.9, and O^{2-} [VI] = 1.4) and Eq. 3, tolerance factor values for each composition can be calculated: $SrCe_{0.9}Y_{0.1}O_{3-\delta}$ (SCY) = 0.883, $SrCe_{0.45}Zr_{0.45}Y_{0.1}O_{3-\delta}$ (SCZY) = 0.9105, $SrZr_{0.9}Y_{0.1}O_{3-\delta}$ (SZY) = 0.939, and $BaZr_{0.9}Y_{0.1}O_{3-\delta}$ (BZY) = 0.996. By replacing Ba^{2+} with Sr^{2+} at the A-site in this study, we fabricate samples with simultaneously lower tolerance factors and lower unit cell volumes than their Ba-containing counterparts, to decouple these contributions to CCE. (By contrast, in the prior study, unit cell volumes increased as tolerance factor decreased.) Bulk strains are measured with dilatometry, and stoichiometry changes are measured with thermogravimetry (TGA). Powder lattice strains, lattice strain anisotropy, proton stoichiometry changes, and B-O-B bond angles are also examined using *in-situ* neutron diffraction at various isotherms and humidities. We aim to determine whether the previously observed opposite trends of tolerance factor and cell volume vs. CCE extend over a larger range, and to observe experimentally the hydration-induced bond angle changes predicted by the earlier DFT calculations.

2. Methods

Each sample was fabricated with the modified Pechini sol-gel route using ZrO(NO₃)₂ (Alfa Aesar, 99.9%), Y(NO₃)₃ (Alfa Aesar 99.9%), Ce(NO₃)₃ (Thermo Scientific 99.99%), Ba(NO₃)₂ (Alfa Aesar 99.99%), and Sr(NO₃)₂ (Alfa Aesar 99.97%), citric acid (Fisher Chemical), EDTA (OmniPur), and ethylene glycol (Fisher Chemical). First, 100 mg of each cation precursor was thermally decomposed and the mass change monitored to calculate accurate molecular weights (including waters of hydration) and reliable cation content for the following steps. Nitrates were first dissolved in DI water under constant stirring, followed by citric acid (CA) and EDTA in the molar ratio 1:1:2 (total transition metals):EDTA:CA. After complete dissolution, the solution was

held at 60 °C for 30 min to promote chelation, and the pH was balanced at 6 by slowly adding ammonia. Ethylene glycol (EG) was then added in the molar ratio 1:9 (total transition metals):EG. The solution was heated above 80 °C until a viscous gel was formed. After drying the gel at 225 °C overnight, the resulting dry gel was calcined at 800 °C for 7 hours, and it was then high energy ball-milled in ethanol for 20 minutes to break up agglomerates. To achieve low density pellets with faster equilibration times, SrCe_{0.9}Y_{0.1}O₃ (SCY), SrCe_{0.45}Zr_{0.45}Y_{0.1}O₃ (SCZY), and SrZr_{0.9}Y_{0.1}O₃ (SZY) were sintered in lab air during 2 stages, first at 1200 °C for 4 hours, and then 1450 °C for 10 minutes. BaZr_{0.9}Y_{0.1}O₃ (BZY) was sintered in lab air at 1600 °C for 14 hours.

Phase purity was examined with room temperature X-ray diffraction (XRD), using a Bruker D8 Advance (Model # D8 Advance A25) with Cu Kα radiation with line focus, 60 mm Göbbel mirror and 0.2 mm divergence slit primary optics, and Dectris Eiger2R_500K detector. A 0.01° step size, 0.1 seconds/ step were used for the 10 -60° 2θ range, and the data were fit with GSAS-II (version 5304). Refinements were performed using the following structure files: ICSD 8385 (BZY), 80272 (SCY and SCZY), and 173398 (SZY). ICSD 80272 and 173398 CIF files were adjusted for the correct cation site fractions, and all files were refined to obtain lattice parameters for relative density (RD) calculations.

Isothermal chemical strains and stoichiometry changes were obtained using dilatometry (Linseis dual push-rod dilatometer L75HD 1600 C) and thermogravimetry (in-house assembled, using Mettler Toledo XPR6UT5 microbalance), respectively. These measurements were taken at 430, 530, and 630 °C by switching between as-received, dry UHP Ar gas and humidified Ar gas with 1.06% H₂O, obtained by flowing the gas through a bubbler chilled to 8 °C. Chemical strain (ε_C) and stoichiometry changes ($\Delta[(OH)_O^*]$) were calculated as,

$$\varepsilon_C = \frac{\Delta L_C}{L_0} \tag{4}$$

$$\Delta[(OH)_O] = \frac{\Delta m/MW_{OH}}{m_i/MW_{comp}} \tag{5}$$

Where ΔL_C is the length change due isothermal gas changes, with $\Delta L_C = 0$ at the most oxidizing condition at each temperature, and L_o is the sample length at room temperature. Δm is the mass change between the two gas atmospheres measured in TGA, m_i is the total starting mass of coarsely ground sample powder, and MW_{OH} and MW_{comp} is the molecular weight of the $(OH)_O^{\cdot}$ ion and of the formula unit of the composition measured, respectively.

In-situ powder neutron diffraction was carried out at time-of-flight (TOF) neutron powder diffractometer POWGEN (BL-11A), located at Spallation neutron source (SNS), Oak Ridge National Laboratory. The Automated Gas Environment System (AGES)[26] was used to allow control of both gas flow and temperatures during in-situ neutron diffraction measurements. A neutron bank with center wavelength of 1.5 Å was employed for data collection in a wide d spacing range from 0.5 Å to 12 Å. Approximately 2 g of powder sample was loaded into the quartz basket. Both the empty quartz basket and the sample were measured at identical temperatures. The neutron signal of the empty quartz basket at each temperature was subsequently subtracted to obtain the neutron diffraction patterns of the sample. For neutron diffraction experiments, the same nominal temperature and humidity conditions as dilatometry and TGA were used. To control the N₂ humidity, the gas flowed through a bubbler set to 8 °C at the humidified condition to achieve 1.06% H₂O, consistent with the conditions for dilatometry and TGA. Untreated UHP N₂ gas was used for the nominally dry condition. (Note: the dew point of the nominally dry condition could in principle be slightly different than in TGA or dilatometry.) Heating rates were all 5 K/min. To avoid excessive run times, however, the schedule was designed differently. Instead of gas changes taken

during isothermal holds, the samples were taken to 630 °C under dry N₂ gas and held for 1 hour before a scan was taken (2-hour scan time); scans were then repeated at 530, 430 and 90 °C in dry N₂. After the scan at the lowest temperature point, the sample atmosphere was switched to humidified N₂ gas, and the same temperature profile, with scans after an hour at each step, was repeated. This isobaric procedure was chosen because chemical equilibrium typically occurs more rapidly after temperature steps than after isothermal pH₂O changes, and a 1-hour dwell before each scan is consistent with prior methodology[6], [27], [28]; however, without time-dependent monitoring we cannot be certain that equilibrium was fully reached at each step. Later TGA measurements on powder samples with isothermal humidity changes demonstrated that longer equilibration times are necessary under gas switching conditions. Refinements of neutron diffraction data were performed using GSAS-II software[29] with POWGEN instrument parameter files. The data were initially refined for lattice parameters and microstructure using the same structure files as listed above for XRD refinement (i.e., those that were modified to include the experimental cation site fractions measured by X-ray fluorescence (XRF, Shimadzu EDX-7000 Energy-Dispersive X-Ray Fluorescence Spectrometer)). Atomic positions and oxygen site fractions were then allowed to refine, followed by atomic thermal parameters. During this process, the refined phases were viewed with calculated and observed Fourier transform isosurfaces using VESTA (version 3.5.8)[30]. Lastly, unaccounted-for negative scattering regions in the observed Fourier transform maps were used as starting positions for hydrogen atoms that were added into the structure files at this stage. Oxygen and hydrogen positions and site fractions were then refined to obtain the final structure and stoichiometry at each condition.

SEM images (JEOL JSM-7000F) were taken to investigate the possible effect of microstructure on bulk CCE. Samples were sanded with sequentially finer grits, until finishing

with a 0.1 µm diamond lapping film, and the samples were thermally etched at 1100 °C for 1 hour to reveal the grain structure. After sputter coating a 10 nm gold layer (Denton Desk II TSC) on the surface, images were taken with the secondary electron detector using a 2 kV accelerating voltage and a 5 mm working distance.

3. Results

3.1 Phase & Microstructure Characterization

Phase purity was determined with XRD pattern matching and Rietveld refinements, with the refinement results shown in Figure 1. The effect of cation substitution is clear; as tolerance factor decreases (BZY > SZY > SCZY > SCY), peak splitting increases, along with the intensity of the first peak at $\sim 21^{\circ}$, as the structure distorts further from the cubic phase. There is a significant increase in peak angles going from BZY to SZY, indicating smaller d-spacings, due to the smaller ionic radii of Sr^{2+} (1.44 Å), relative to Ba^{2+} (1.61 Å). Then as $[Ce^{4+}]$ (0.87 Å) increases and $[Zr^{4+}]$ (0.72 Å) decreases, the d-spacing increases again from SZY to SCY. Refined cell volumes per formula unit, in descending order, are SCY = 78.822 Å³, SCZY = 74.038 Å³, BZY = 74.319 Å³, $SZY = 69.505 \text{ Å}^3$. While the proton concentration of these as-prepared samples is unknown and can affect the cell volumes, the relative changes in pseudocubic lattice parameter from varying cation composition (Sr vs. Ba, Ce vs. Zr) are about an order of magnitude larger than relative lattice parameter changes from varying proton concentration in the accessible range in this study (shown later). The peaks in SCZY appear broader than those of the other compositions; this is largely attributed to multiple reflections that are closely spaced at each peak. Refined crystallite sizes returned values > 100 nm for all compositions, regardless of the starting value.

Microstructure is expected to influence measured CCEs. Initial samples had relative densities (RD), in ascending order: BZY (60%) < SCZY (71%) < SZY (73%) < SCY (78%).

Samples were intentionally fabricated at intermediate RD to improve hydration/dehydration reaction kinetics, which are typically very slow for dense electrolytes. Due to unexpected trends in strain and CCE, discussed later, replicate samples of SZY and SCZY were also fabricated and measured, and their relative densities were SZY = 62% and SCZY = 68%. The replicate samples were intentionally made less dense to determine how porosity might affect CCE, although the difference in RD for SCZY is not as pronounced.

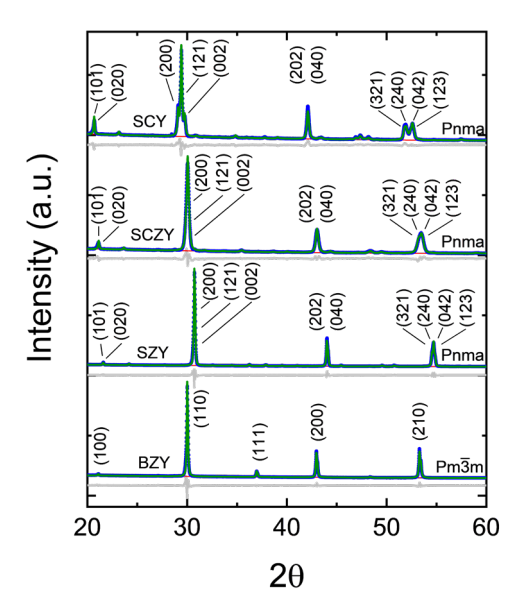


Figure 1: Room temperature, Cu K α X-ray diffraction patterns and refined profiles. Intensities (linear scale) are normalized by maximum peak intensity and offset for clarity. Observed data points are shown as blue circles, refined profile in green, background in red, and difference profile in grey.

3.2 Bulk Hydration Coefficients of Chemical Expansion

As a representative example of the isothermal, time-dependent strain and mass relaxation responses to changes in pH₂O, raw dilatometry and TGA data for BZY at 630 °C were converted to percent chemical strain ($\%\epsilon_C$) and percent mass change ($\%\Delta m$), respectively, and shown in Figure 2. These data include some of the more rapid equilibration steps, taking only about 5 hours during hydration, and about 50 hours during dehydration to reach steady state (for dilatometry). SCY had some of the longest equilibration times, requiring over 150 hours at 630 °C. Equilibration

times in the TGA are typically faster due to the sample being a coarse powder, rather than a porous bar, and the smaller sample chamber in our TGA lends itself to faster gas exchanges.

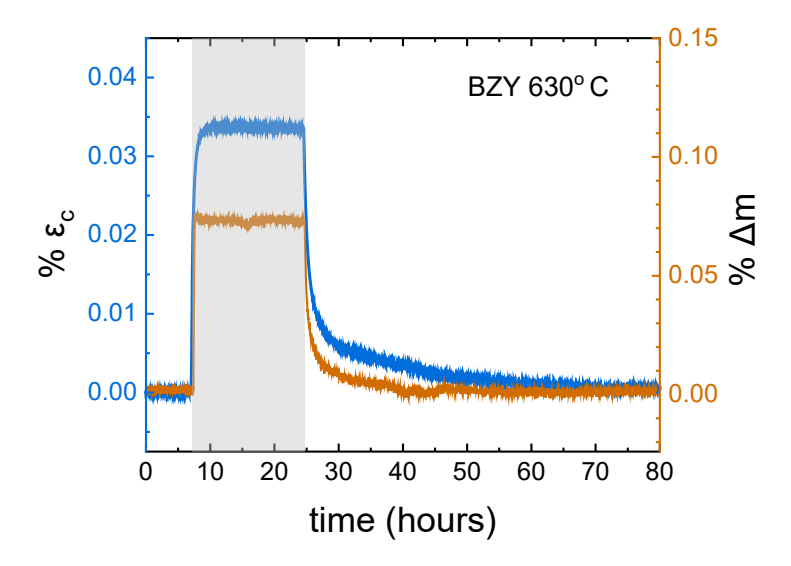


Figure 2: Percent strain in blue, from dilatometry, and percent mass change in orange, from TGA, during isothermal pH₂O changes, where the reference 0% value is the nominally dry condition at this isotherm. In the shaded region, the sample is exposed to a hydrated Ar atmosphere with 1.06% H₂O, and the unshaded region has no added H₂O to the Ar gas stream.

Values of chemical strain and stoichiometry changes calculated from the measured data for all compositions are shown in Figure 3a and Figure 3b, respectively. Initial measurements on SZY reveal exceptionally low strains and hydration CCEs, and measured values for SCZY are not quite intermediate between SCY and SZY. For these reasons, replicate samples were fabricated and measured, both of which have lower densities than the initial samples (although the difference is slight in SCZY). For both initial and replicate samples, SCZY exhibits similarly large strains. The second sample of SZY, with lower relative density, exhibits significantly larger strains and stoichiometry changes than those of the initial sample.

The data from Figure 3a and Figure 3b are used to calculate hydration CCEs, using Eq. 2, and these results are shown in Figure 4. While SCY has the lowest measured strain, the low

stoichiometry changes result in relatively large CCEs, being close to SCZY for all temperatures. Surprisingly, SCZY exhibits large strain and stoichiometry changes that often exceed the values of SCY and SZY, despite being an intermediate composition between these two. CCEs tend to increase slightly or remain invariant with decreasing temperatures, with the exception of the local minimum for SCY at 530 °C. Across the three temperatures measured, the average hydration CCEs increase in the order SZY = 0.0174, BZY = 0.0398, SCY = 0.0523, and SCZY = 0.0528. Despite the variation between replicates in SZY, the larger observed hydration CCEs in the second sample are still lower than the CCEs measured in the other three samples. In this work, CCE values for BZY have good agreement to the values of BZY obtained by Chen et al.[31], but the trend with temperature is inverted. Fujisaki et al.[32] used XRD and TGA to determine volumetric coefficients of chemical expansion ($\beta_{\text{chem}} = (\Delta V_{\text{lattice}}/V_{\text{lattice}}) / [\text{OH}]$), and they also observed larger values for SCY ($\beta_{chem} = 0.16 - 0.19$) than for SZY ($\beta_{chem} = 0.04 - 0.041$). The changes in stoichiometry by Fujisaki also agree with the trends in our work for SCY and SZY. The direct comparison of values between their work and ours, however, may be misleading due to a difference in Y dopant concentration and in methodology. The most notable differences in methodology include the use of isothermal pH₂O changes in this work vs. isobaric temperature changes in their work, and smaller values of pH₂O used in this work.

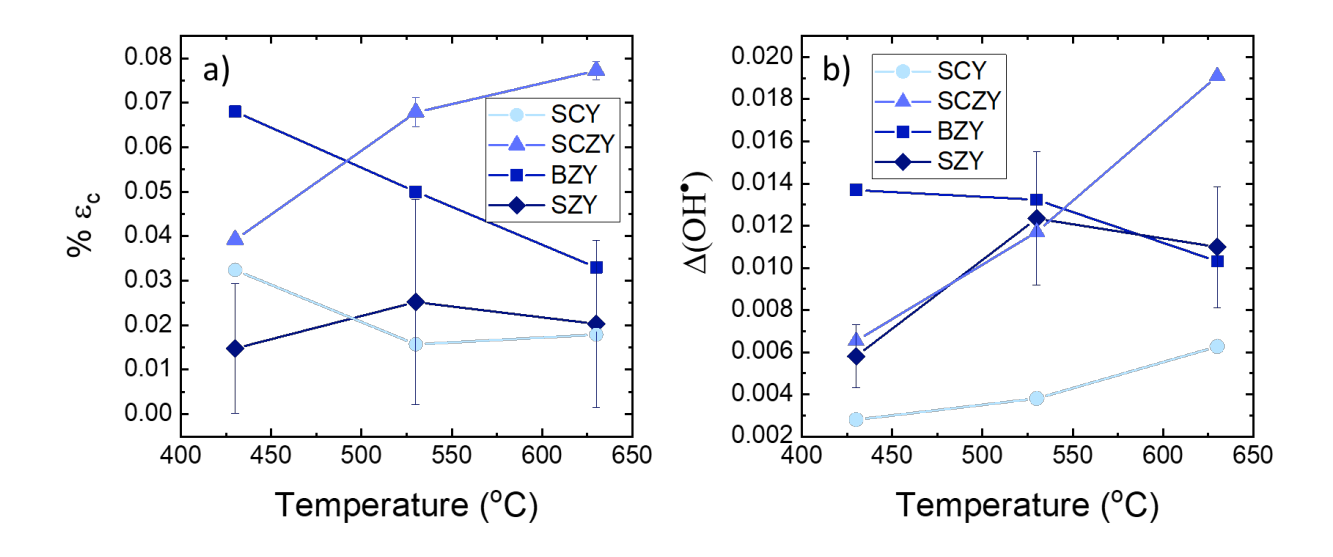


Figure 3: Data from dilatometry and TGA, converted to a) isothermal percent chemical strain (humid vs. dry) and b) isothermal stoichiometry change (humid vs. dry), respectively, at each temperature studied. (The nominally dry value is the 0 reference point for strain and stoichiometry at each isotherm.) Error bars for SZY and SCZY compositions reflect the standard deviation in replicate samples with varied microstructures.

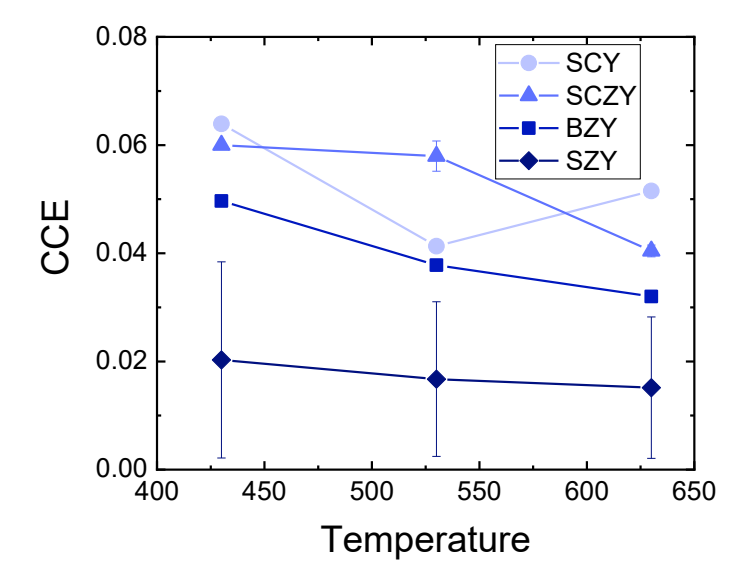


Figure 4: Hydration CCEs determined from dilatometry and TGA measurements for each composition, measured at 430, 530, and 630 °C. Error bars for SZY and SCZY compositions reflect the standard deviation in replicate samples with varied microstructures.

To help identify trends, CCEs from this work and from the prior work by Chen et al.[5] are plotted vs tolerance factor (Figure 5) and vs. pseudocubic lattice parameter (Figure 6). The

pseudocubic lattice parameters (a_{pc}) in Figure 6 are calculated using Eq. 6 to avoid overestimating the lattice size of the lower symmetry phases that have more than one formula unit per unit cell.

$$a_{pc} = \left(\frac{V}{N}\right)^{1/3} \tag{6}$$

Where V is the refined unit cell volume at room temperature and N is the number of formula units per unit cell (e.g., the Pnma structure has 4 formula units). In Figure 5, the data appear to take on an inverted volcano shape, indicating that there may be an optimized tolerance factor value for low hydration CCE in the range t = 0.93 - 0.95. Interestingly, BaCe_{0.9}Y_{0.1}O₃ (BCY) and SrZr_{0.9}Y_{0.1}O₃ (SZY) have nearly identical values of tolerance factor (BCY: 0.936, SZY: 0.939), and both have the lowest hydration CCE for their respective solid solution (BCY: 0.0010-0.0190, SZY: 0.0152-0.0203), despite a different primary cation at both the A- and B-site. A second-order polynomial function is fit to all data in Figure 5, and this is represented by the dark grey line. Nearly all data fall within the shaded region, but SCY and SCZY have some outlying values.

Figure 6 does not reveal as consistent of a dependence of hydration CCE on room-temperature pseudocubic lattice parameter (a_{pc}). The correlation of increasing hydration CCE with decreasing a_{pc} observed in the work of Chen et al. in the BZY-BCY solid solution does not extend to the SCY-SZY solid solution; in fact, the trend for perovskites with Sr on the A-site is almost the opposite of those based on Ba, with hydration CCE increasing as a_{pc} enlarges. Although it is perhaps more intuitive to imagine that an ion of potentially consistent size ($(OH)_0$) that is inserted into a smaller lattice volume will always result in a larger strain, the trends in Figure 5 and Figure 6 suggest this idea is not borne out consistently. Rather, tolerance factor is the more predictive metric for CCE.

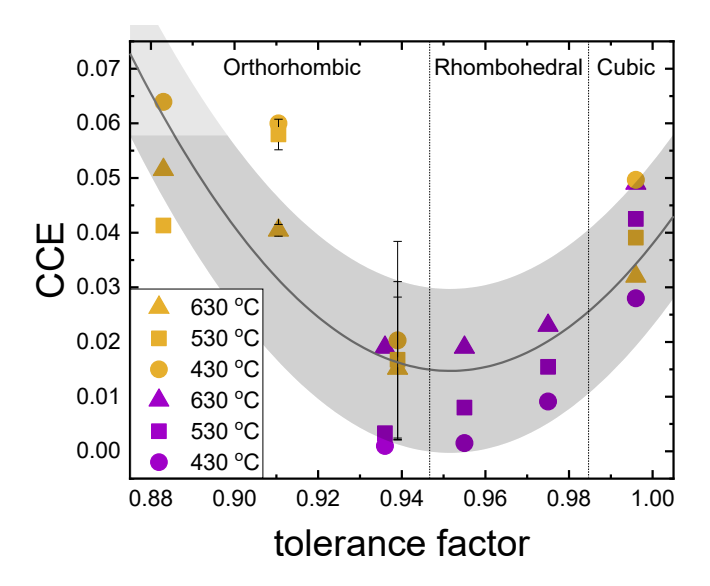


Figure 5: CCEs (determined from dilatometry and TGA measurements) plotted against tolerance factor for the compositions measured in this work (orange) and those measured previously by Chen et al. (purple)[5]. The solid grey line is a best fit polynomial of both this work and prior work, with the light grey region serving as a guide to the eye. Error bars for SZY and SCZY compositions reflect the variation in replicate samples with varied microstructures.

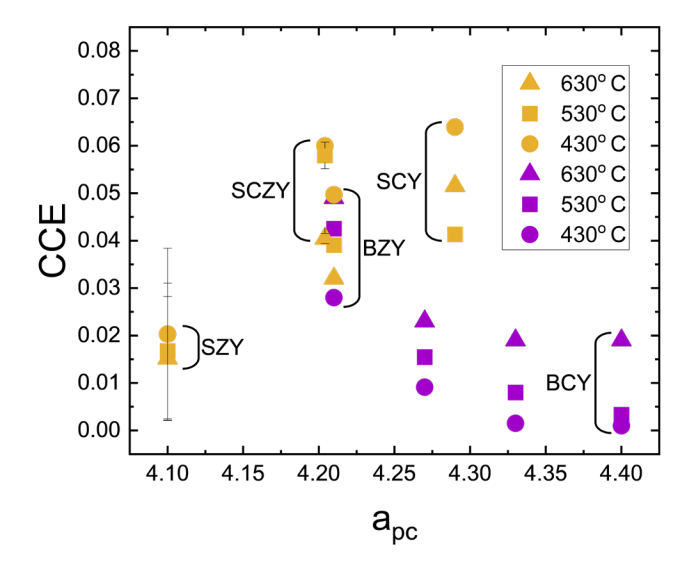


Figure 6: Hydration CCEs (determined from dilatometry and TGA measurements) plotted against measured room-temperature pseudocubic lattice parameters for the compositions in this work (orange) and those measured previously by Chen *et al.* (purple). Error bars for SZY and SCZY compositions reflect the variation in replicate samples with varied microstructures.

3.3 In-situ Neutron Diffraction

Further insight into hydration-induced strains at the atomistic-to-unit cell length scales derives from in-situ neutron diffraction (ND). Unlike XRD, ND is appropriate to determine positions and site occupancies of light atoms O and H, providing further observations of how hydration affects lattice distortions. Refined TOF data plots at 530 °C in the humidified condition for each sample are shown in Figure 7, and refinement data for all samples at each condition are reported in Table S1. The resulting lattice parameters from refinements at all temperatures are presented in Figure 8 for both the dry gas ($\sim 0\% H_2O$) and humidified gas (1.06% H_2O) conditions. All unit cell axes expand after hydration except the c-axis in SCY, which demonstrates a very small contraction. The crystallographic axis-resolved chemical strain (isothermal strain upon increasing from ~0% to 1.06% H₂O in the gas) from ND refinements in Figure 9 illustrates the anisotropic strain in SCY and SZY. Both compositions exhibit differing strains along each axis, with the magnitude of these strains following the trend b > c > a. BZY chemical strains are also shown here, but because this composition crystalizes in the cubic structure, the lattice strain is observed to be isotropic along the orthogonal axes by the ND refinements. We attempted to fit the BZY data in the orthorhombic structure to determine any subtle strain anisotropies or changes in the B-O-B bond angles, but these attempts produced negligible changes in the fitting results. Fitting BZY in the cubic structure is also supported by the lack of any emergent peaks in the diffraction profile that would indicate a lower symmetry phase. SCY clearly has the most anisotropic hydrationinduced strain, visualized by the small negative (compressive) a-axis strain at 430-530 °C, and near zero a-axis strain at 630 °C. Due to the positive valued (tensile) strains at the b- and c-axes for both compositions, we can quantify the chemical strain anisotropy between these axes by taking a ratio of their strain magnitudes, b/c. This ratio returns values of 1.21-1.39 for SZY and 1.37-2.06 for SCY.

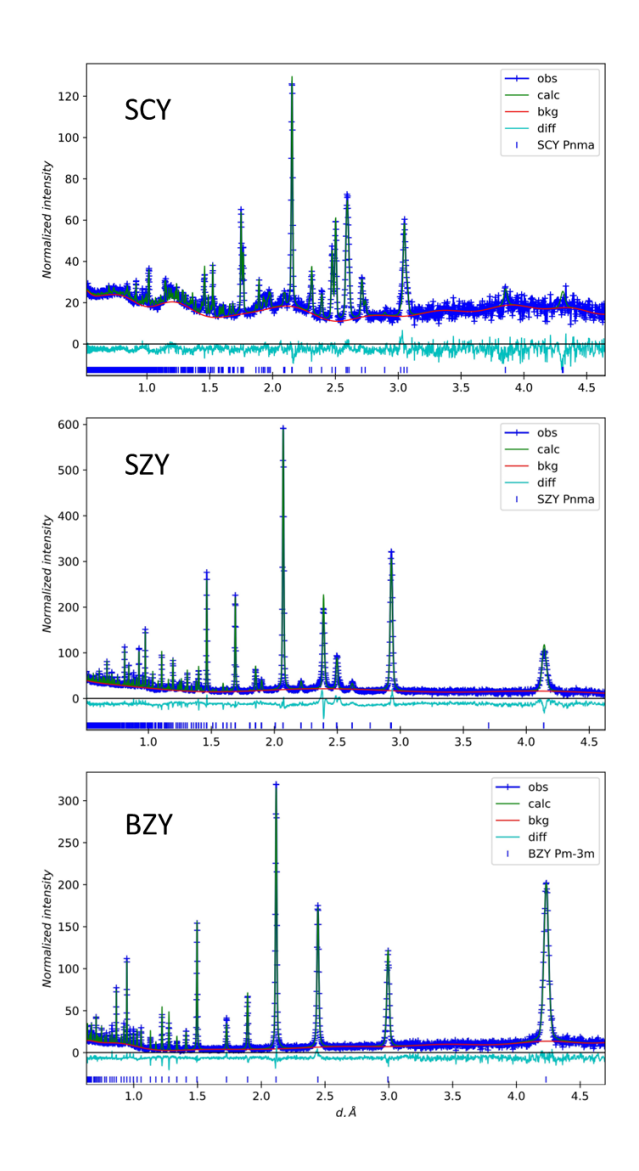


Figure 7: Rietveld refinements and difference profiles (observed - calculated) for each sample at 530 °C in the humidified condition.

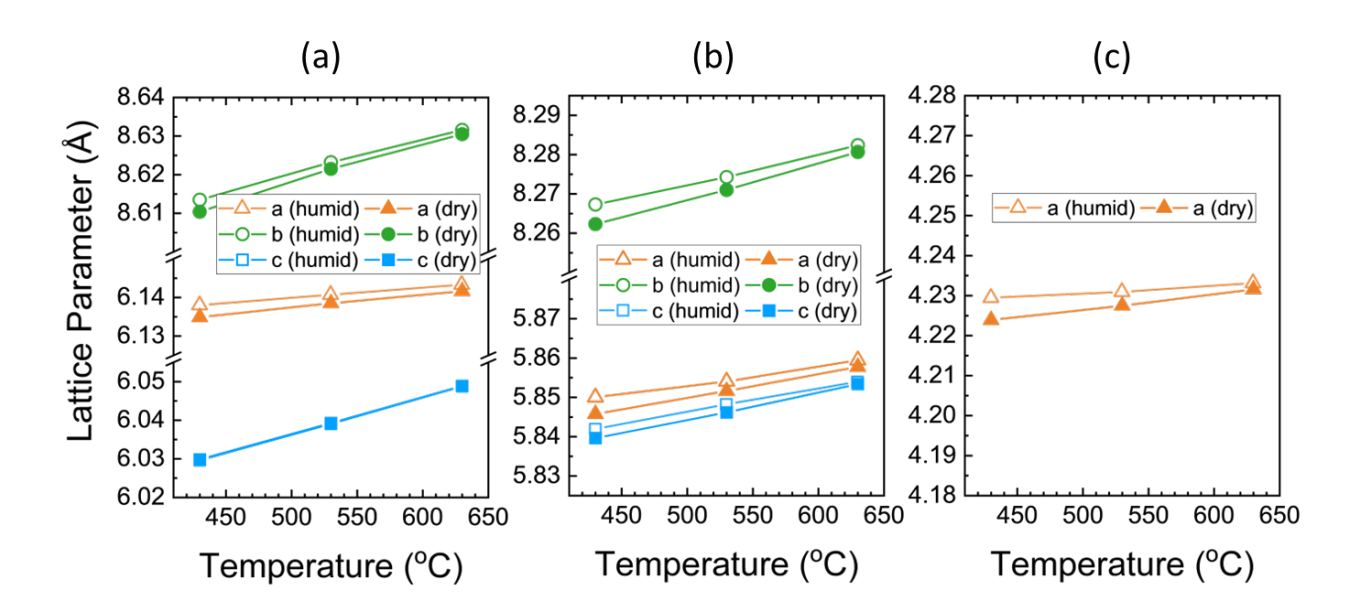


Figure 8: Lattice parameters determined by neutron diffraction pattern refinement at the nominally dry gas (~0% H₂O) and humidified gas (1.06% H₂O) conditions for a) SCY, b) SZY, and c) BZY powders. Axis labels are consistent with the *Pnma* structure for both SCY and SZY compositions.

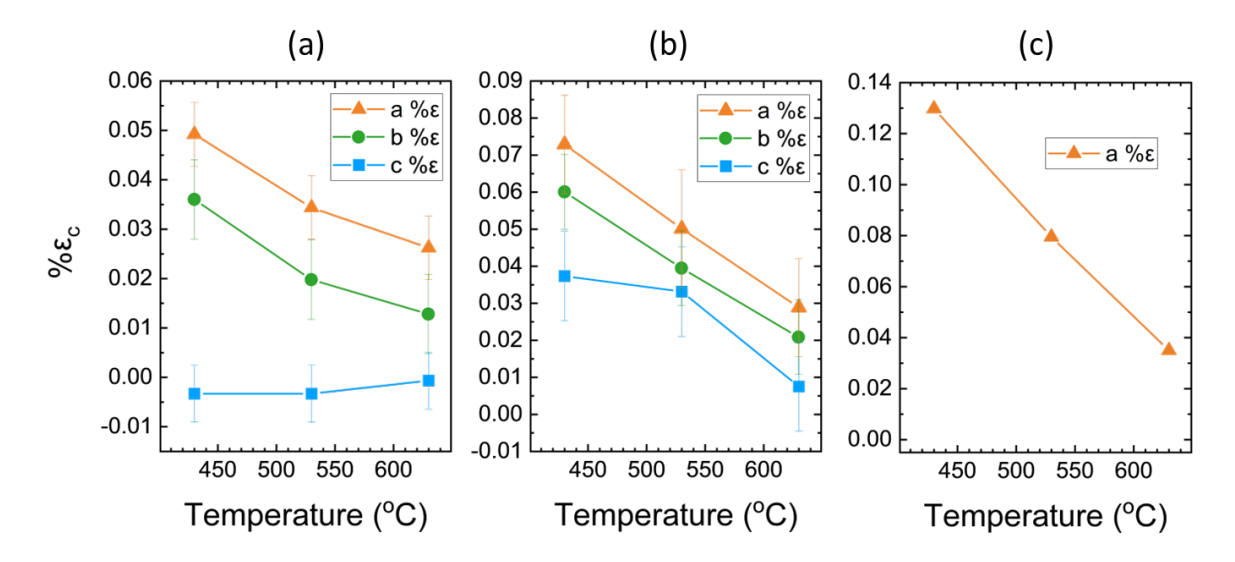


Figure 9: Lattice-resolved isothermal chemical strains upon increasing from nominally $\sim 0\%$ to $\sim 1.06\%$ gaseous H₂O for a) SCY, b) SZY, and c) BZY powders, determined by neutron diffraction pattern refinement. Axis labels are consistent with the *Pnma* structure for both SCY and SZY compositions, where unit cell lengths follow the trend b > a > c. Error bars are calculated from lattice parameter refinement uncertainties (given in SI), propagated in accordance with strain calculations.

Neutron diffraction refinements of oxygen positions also reveal how hydration affects the B-O-B bond angles, as seen in Figure 10. The bond angle naming convention used by Cammarata

et al.[33] is used here, where θ_z corresponds to the B-O-B angle along the c-axis, and θ_{xy} is the B-O-B bond angle in the a-b plane (for the orthorhombic structures). Cation substitution of Zr for Ce, at the B-site, results in an increase in both θ_{xy} and θ_z due to the higher symmetry of SZY, though the change in θ_z is much more significant (~13%) than the change in θ_{xy} (~5%). The bond angles in both compositions increase toward 180° with increasing temperature for both dry and humid conditions, which is expected as the temperature increase drives each phase toward higher symmetry. Upon hydration, SCY exhibits almost no change in bond angles, while SZY has a notable decrease in θ_z . A decrease in bond angle after hydration is consistent with DFT predictions from Chen et al[5].

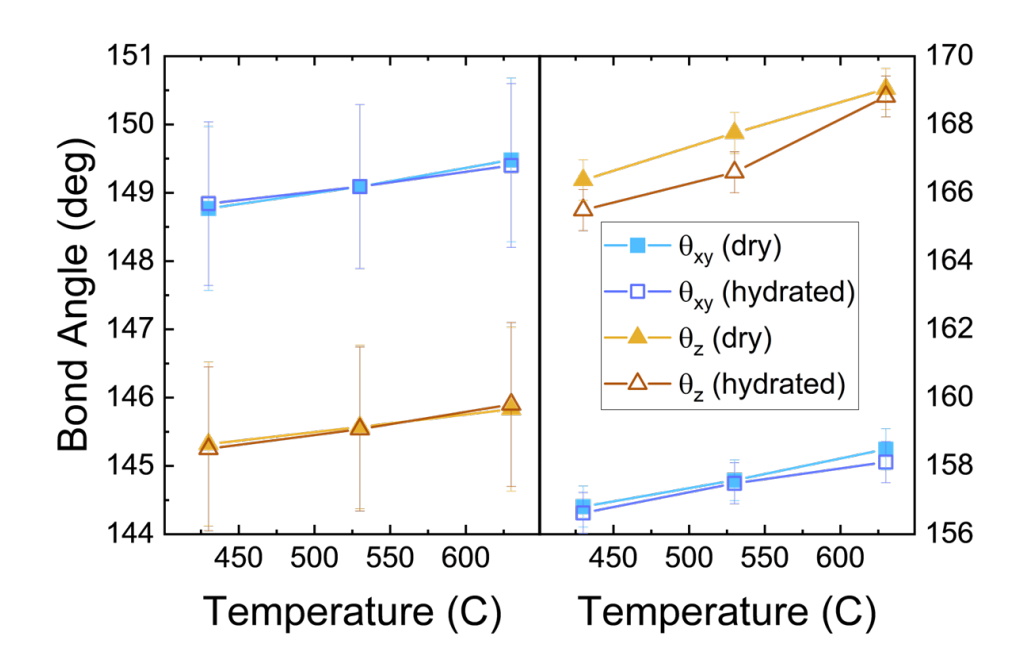


Figure 10: B-O-B bond angles of a) SCY and b) SZY, as determined by neutron diffraction refinements (note: "dry" and "hydrated" are relative, not absolute terms). BZY refined best to 180° B-O-B angles for both the nominally dry and hydrated gas conditions and is not shown. Error bars are calculated from angle changes caused from atomic displacements that reflect oxygen position errors calculated during refinement (SCY: $\sigma_{xyz} = 0.002$, SZY: $\sigma_{xyz} = 0.001$).

A summary of interatomic B-O bond distances, in Å, is presented in Table 1. SCY and BZY behave largely as expected: bond distances increase with increasing temperature and hydration.

SZY bond distances, however, are largely independent of temperature. Thermal expansion of the SZY lattice is primarily caused by increasing B-O-B bond angles (see Eq. 6 in section 4.1), supported by the larger temperature dependence of bond angles in Figure 10.

Table 1: B-O bond distances, in Å, from neutron diffraction refinements at 630, 530 and 430 °C.

Temperature	SCY (dry)		SCY (hydrated)		SZY (dry)		SZY (hydrated)		BZY (dry)	BZY (hydrated)
(°C)	Ce - O1	Ce - O2	Ce - O1	Ce - O2	Zr - O1	Zr - O2	Zr - O1	Zr - O2	Zr - 01	Zr - O1
630	2.25(7)	2.23(2)	2.26(0)	2.23(8)	2.08(0)	2.10(7)	2.08(0)	2.10(9)	2.11(6)	2.11(7)
530	2.25(4)	2.23(4)	2.25(7)	2.23(5)	2.08(0)	2.10(8)	2.08(3)	2.10(9)	2.11(4)	2.11(5)
430	2.25(3)	2.23(3)	2.25(4)	2.23(3)	2.08(0)	2.10(8)	2.08(3)	2.11(1)	2.11(2)	2.11(5)

Structure model visualizations obtained from refining against the structural data at 530 °C are displayed in Figure 11. As the tolerance factor decreases from right to left (BZY to SCY), there is an increasing deviation from the cubic phase as B-O-B bond angles decrease in magnitude (away from 180°). The refined hydrogen positions occupy interstices in the lattice, near octahedral face centers. It is important to note that the high mobility of protons in the temperature range studied introduces uncertainty in the refined hydrogen positions; however, the positions remained stable through multiple refinement iterations. The visualization of Fourier Transform isosurface maps using VESTA (Figure 12) supports the refined hydrogen positions. Hydrogen atoms have a negative scattering length, and the negative scattering regions (blue isosurfaces) match well between the calculated maps and the observed maps, shown for SCY in Figure 12b and Figure 12c, respectively. SZY had the shortest H-O bond length at 1.324 Å, followed by SCY at 1.665 Å and BZY at 1.831 Å.

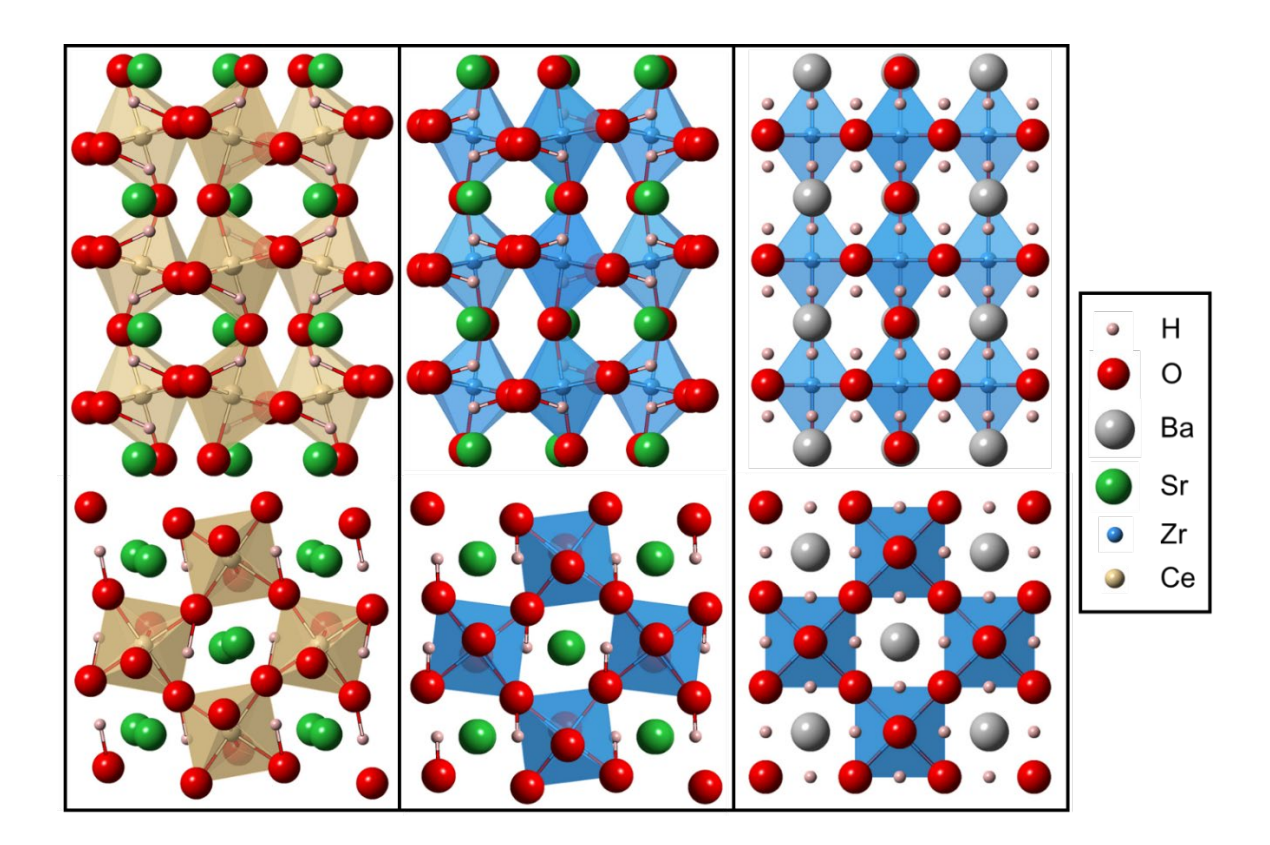


Figure 11: Visualization of the structure model based on refined atomic coordinates from neutron diffraction at 530 °C in humidified N₂ (1.06% H₂O) for SCY (left), SZY (center), and BZY (right). The top images have view directions (100), (010), and (110) from left to right, and the bottom images have view directions (001), (010), and (110) from left to right. All images include atoms extended beyond the unit cell to match dimensions and to visualize octahedra.

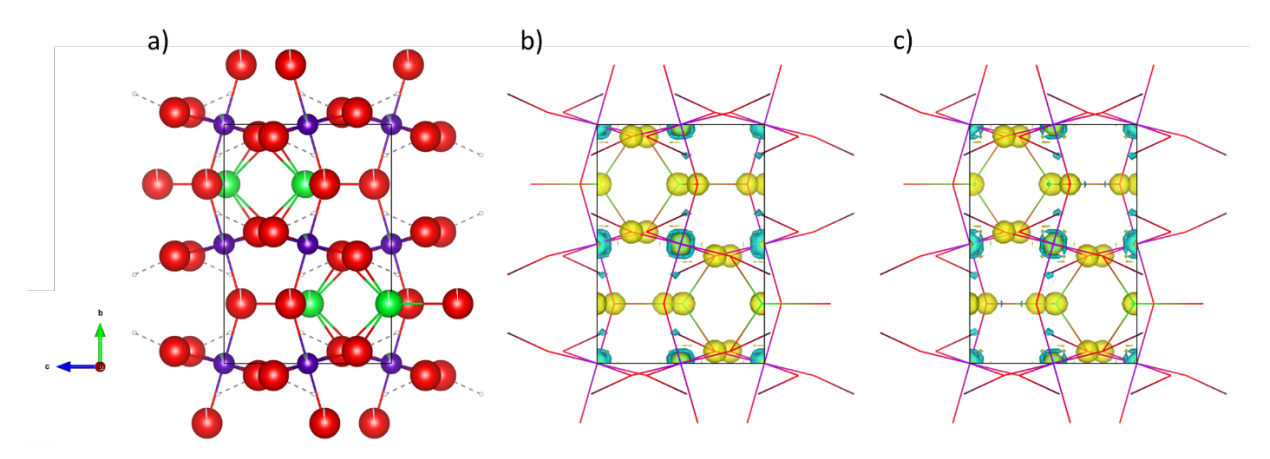


Figure 12: a) Visualization of the refined lattice of SCY and atomic positions at 530 $^{\circ}$ C (O = red, Ce/Y = purple, Sr = green, and H = white) in comparison to b) the calculated Fourier Transform isosurface map from the same refinement. c) The observed Fourier Transform isosurface map from the experimental data. In b) and c), positive scattering regions are shown in yellow, and negative

scattering regions are shown in blue. The wireframe within the isosurfaces corresponds to the atomic bonds in a).

4. Discussion

The prior work by Chen et al[5]. that motivated this study demonstrated a monotonic decrease in hydration CCE as the tolerance factor, t, decreased in the proton-conducting BaCe_{0.9-x}Zr_xY_{0.1}O₃ solid solution (over the t range 0.996 – 0.936). Our synthesis and measurement of the prototypical proton-conducting material, BZY, in the current work gave very similar values of CCE to those reported in the prior study. Newly determined CCE vs. t for the SrCe_{0.9-x}Zr_xY_{0.1}O₃ solid solution (t range 0.939 – 0.883) in this work, together with the prior work, enables us to now study the trend across a much wider range of t values. Taken together, the new and prior data suggest a U-shaped relationship between hydration CCE and t. SZY, with an intermediate t value of 0.939 (the highest in the current Sr-containing solid solution), exhibits the lowest hydration CCE in the SCY-SZY solid solution. To help understand the observed CCEs in the compositions studied, we discuss the potential influence of octahedral tilting, unit cell size, effective oxygen vacancy radius, lattice strain anisotropy, microstructure, and absolute proton concentration in addition to the calculated tolerance factors.

4.1 Tolerance Factor and Octahedral Tilts

Figure 5 reveals the presence of a (local) minimum in the U-shaped hydration CCE vs. t plot at t = 0.93 - 0.95. SZY, which sits at this local minimum, also undergoes the most significant decrease in its B-O-B bond angles among the SZY-SCY-BZY series when hydrating. A decrease in these bond angles upon hydration likely contributes to mitigating the material's overall volume expansion. As demonstrated by Glazer, in work classifying octahedral tilts in perovskites[34], the lattice parameters are directly related to these tilt angles, where increasing tilts (decreasing B-O-B

bond angles) decrease the pseudocubic lattice parameters (a_p, b_p, c_p) for a given anion-anion distance (ξ) .

$$a_p = \xi \cos(\beta) \cos(\gamma)$$

$$b_p = \xi \cos(\alpha) \cos(\gamma) \tag{7}$$

$$c_p = \xi \cos(\alpha) \cos(\beta)$$

 α , β , and γ denote the angles of tilt about [100], [010], and [001], respectively (0° tilt at a 180° B-O-B bond angle).

The tendency for inserted ions to be partially accommodated by structural distortions like octahedral tilting may also be influenced by space group and bond strength. The low symmetry of the orthorhombic space groups, relative to rhombohedral and cubic space groups, offers fewer restrictions in ionic displacements and in tilt systems. For example, the orthorhombic space group Pnma with the $a^*b^+b^+$ tilt system supports two tilt magnitudes, one in phase and two out of phase, while the rhombohedral space group $R\overline{3}c$ with $a^*a^*a^*$ tilt system has only one tilt magnitude along each axis, all being out of phase. The cubic systems have no tilts. Space group symmetry may therefore limit how ions are incorporated, with the cubic structure being limited to increasing bond lengths in the extreme case (in reality, small local distortions likely exist). This "flexibility" in ionic incorporation for orthorhombic structures is also supported by the large $\Delta[(OH)_O^*]$ observed in SZY. Bond stiffnesses are expected to influence the tendencies for bond elongation and/or bond angle changes, but consistent trends between elastic moduli and hydration CCE are not evident in this work. Bulk moduli for BZY (140 GPa) and SZY (152 GPa) are significantly higher than the values for BCY (105 GPa) and SCY (115 GPa)[5], [35], yet the latter two have the lowest and

highest CCEs of these compositions, respectively. However, the minimal B-O bond length changes for SZY may be due to the high bond strength between Zr and O.

4.2 Unit Cell Size

Comparing the SCY-SZY solid solution in this work with the BCY-BZY solid solution in the prior work, SCY-SZY have larger hydration CCEs, on average, than BCY-BZY, although there is significant overlap between SCZY and BZY, which have very similar unit cell sizes. Normalizing length changes by a smaller unit cell (with Sr^{2+} substitution for Ba^{2+}) can contribute to larger CCEs due to larger chemical strains; however, the CCE vs. a_{pc} trend for SCY-SZY in Figure 6 is opposite that of BCY-BZY, where the hydration CCEs increase with increasing unit cell size for the Sr-based compositions.

For the two solid solutions examined in this work, the lack of a consistent trend between CCE and a_{pc} indicates that other crystal chemical factors have more influence on chemical expansion, or there are properties that change with unit cell size which, in turn, influence chemical expansion. An optimized tolerance factor (section 4.1) and/or microstructure/RD (section 4.5) likely impact CCE, and these contributions may outweigh any effects from changing unit cell size. However, chemical substitution and changing unit cell size affects atomic ordering, as seen in Figure 11 and discussed in section 4.1. Atomic arrangements, lattice distortions, and unit cell size can influence the size and shape of ions and oxygen vacancies[24], [36], supported in this work by the smaller Zr-O distances in SZY than BZY (Table 1). The effective sizes of O_0^{\times} , $(OH)_0^{\bullet}$, and v_0^{\bullet} will influence the magnitudes of the competing expansion $((OH)_0^{\bullet})$ replacing v_0^{∞}) and contraction $((OH)_0^{\bullet})$ replacing O_0^{\times}) mechanisms, and the shape of each species is expected to influence the degree of anisotropic expansion. While ions can experience deformation, oxygen vacancies that

lack mass can exhibit more significant changes to their size and shape, and the effects of oxygen vacancy modifications are discussed in more detail.

4.3 Oxygen Vacancy Size

DFT calculations from Chen et al.[31] include results for oxygen vacancy Voronoi volume for two endmember compositions, Y-doped BaCeO₃ and BaZrO₃, and these results suggest that increasing vacancy size may help to lower CCE. For hydration-induced chemical expansion, the lattice strain is primarily explained by the difference in ionic sizes between product ions and reactant ions in Equation 1. The estimates for these ionic sizes vary, but it is generally agreed that the relative ionic sizes follow the order, $O_0^{\times} > (OH)_0^{\bullet} > v_0^{\bullet \bullet}$. The slight contraction caused by the positively charged proton on an oxygen lattice site is smaller than the expansion caused by the $(OH)_0^{\bullet}$ ion filling the vacancy, leading to an overall expansion. The 25% increase in vacancy volume in BCY, relative to BZY, should reduce the difference in ionic sizes between $(OH)_0^{\bullet}$ and $v_0^{\bullet \bullet}$, leading to a smaller net strain.

Fujisaki et al.[32] also demonstrate how changing oxygen vacancy radius can affect CCE for Y-doped SrCeO₃ and SrZrO₃. The authors find that the association of Y dopant atoms can significantly affect vacancy radius, with Y atoms that are close together (Y-O-Y bonding) leading to a larger vacancy radius (1.69 Å), and the distant Y atom configuration leading to a smaller vacancy radius (1.24 Å), both in SCY. The volumetric chemical expansion with the smaller of these two radii resulted in a 3-fold increase in CCE, relative to the case with larger ionic radius. Y-doped SrZrO₃ on the other hand, had a slightly lower volumetric expansion coefficient (β_{chem} = 0.032) with distant Y atoms, which causes a small decrease the vacancy radius (1.24 Å), relative to the larger radius (1.30 Å) when Y atoms are close together (β_{chem} = 0.045). In the case of distant Y atoms, both SCY and SZY have the same vacancy radius, but SCY has a much larger expansion

coefficient than SZY at this condition. Despite SCY having equal vacancy radius and a larger initial unit cell volume, the larger β_{chem} indicates that another factor dominates the CCE response between these two materials. It is worth noting that the configuration with dopant atoms close together is energetically favorable for both compositions, yielding a larger vacancy radius for SCY than SZY. The larger CCE for SZY than SCY at this condition agrees with expectations related to vacancy radii, but this trend in CCE is not consistent with the experimental work. The authors point to bulk elastic modulus as being a contributory factor because SCY has a lower modulus than SZY, leading to larger expansions in the former; however, BCY also has a lower modulus than BZY, but it exhibits a much lower CCE, seemingly contradicting this hypothesis.

4.4 Strain Anisotropy

Figure 9 shows that strain anisotropy increases with decreasing tolerance factor, with SCY even exhibiting contraction along the b-axis. High strain anisotropy has been suggested as a factor that can lead to lower redox CCEs in polycrystalline samples, but this contribution appears to be overshadowed by other factors in this work, since the hydration CCE vs. chemical strain anisotropy trend is not monotonic. In the prior work by Chen et al., BCY exhibited anisotropic strain, with smaller strains in the bulk sample bars than in the powder samples. This effect was attributed to neighboring grains constraining the expansion of one another as they expand with different magnitudes in each direction for the bar, while the powder was free to expand. While this effect may still be present, highly anisotropic expansion did not significantly lower the macroscopic hydration CCE of bulk SCY. SCY also had the highest relative density of the samples measured, and higher densities are expected to enable this constraining contribution as a higher fraction of grains should be contacting others.

4.5 Microstructure

The field currently lacks a comprehensive study relating microstructure to CCE. Trends may be expected to be analogous to those observed for coefficients of thermal expansion (CTE), which are, however, contradictory in literature. Some reports show higher CTE with increasing density[37], [38], and some show lower CTE with increasing density[39]. Increasing grain size sometimes decreases CTE[40], [41], but grain size has also been shown to have no effect on CTE in Ca, Mg, and Al oxides[42]. When present, grain size effects have been attributed to features such as grain boundaries, impurities, and increasing microcracks with increasing grain size. In the prior work by Chen et al., strongly anisotropic BaCe_{0.9}Y_{0.1}O₃ exhibited significant variation in measured CCE in replicate samples with different microstructures, and strains were larger in loose powders, measured with XRD, than in bulk samples, measured with dilatometry. This difference between loose powder and bulk sample strains was attributed to a loose powder being free to expand, while the bulk sample is more constrained by the interfacial bonding between neighboring grains. However, this difference may also be influenced by the measurement method itself; XRD is able to capture the lattice expansion of the crystallites, but it does not necessarily capture the interactions between them. For example, an expansion into pore volumes could serve to decrease observed strains in dilatometry, and samples with high internal surface area may accommodate more strain within pores.

For the bulk, polycrystalline samples studied in the present work, the microstructural aspects that can, in principle, affect CCE include the density, grain size, and pore structure, and their impact may depend on crystal symmetry. Analyzing the microstructure of each sample with SEM (Figure 13) supports the refinement results of grain sizes being larger than 100 nm, but (based on analysis of multiple regions and looking carefully for grain boundaries in dense regions) all samples appear to exhibit a distribution of grain sizes, with some being 100-300 nm, and others

being on the order of 1 μ m. BZY, SZY, and SCZY appear to be largely mesoporous (3-50 nm) with microporous (> 50 nm) regions, while SCY appears to be more dense and largely microporous. The relative densities (RD) from mass and geometry measurements increase in the order, BZY (60%) < SZY (62%) < SCZY (68%) < SCY (78%) for the original samples, and their measured CCEs increase in the order SZY < BZY < SCZY < SCY. The SZY replicate with higher density (73%) exhibited very low strains, contrary to the trend across compositions, and SCZY replicate samples exhibited very consistent strains, despite the slight difference in density (68% and 71%). In other words, no trend can yet be discerned across this full composition range. A future study exploring the effects of grain size, density, pore size, and pore distribution on CCE could be beneficial.

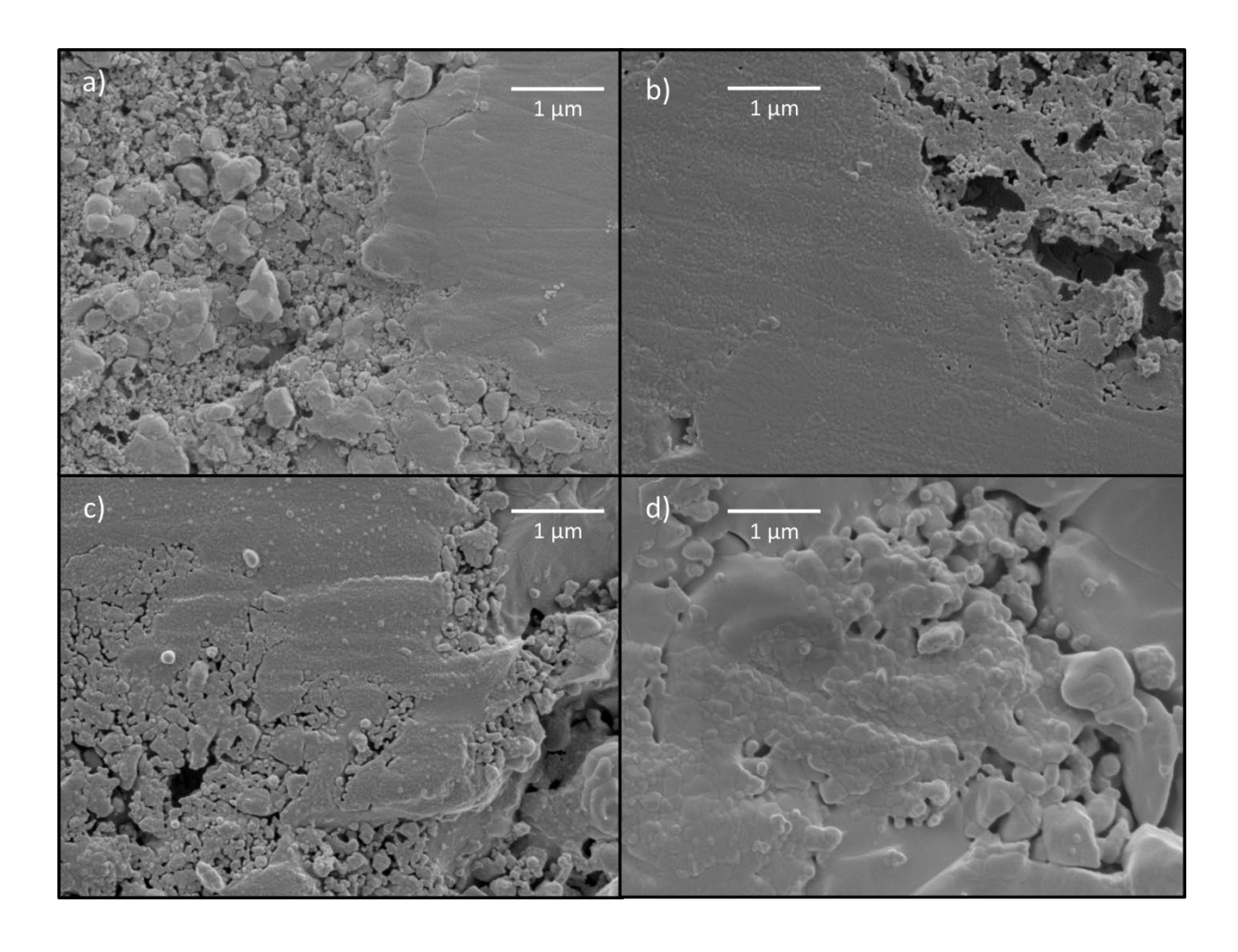


Figure 13: Scanning electron micrographs after thermal etching for porous a) BZY, b) SZY, c) SCZY, and d) SCY ceramics.

4.6 Absolute Proton Concentrations

One emphasis within the present work has been providing accurate measurements of proton concentration *changes*, rather than assuming full hydration/dehydration according to the acceptor dopant concentration, in order to provide quantitative CCEs. In principle, the *absolute* proton concentration could influence CCE *if* both chemical strains are strongly nonlinear with proton concentration *and* proton concentrations are strongly varying across the composition range. To evaluate any role of absolute proton concentration, we examined goodness-of-fit in ND refinements with various H site fractions constrained for the three compositions measured. In every

case, the best fits were obtained with high rather than low H concentrations for both the nominally dry and humid conditions, with H occupancy increasing only slightly for the humid case, consistent with TGA results showing only small changes in H content upon switching the pH₂O. However, when H site occupancy was not constrained (see Supporting Information Table S1), it refined to an unphysically large value well above the acceptor concentration for the Ba and Sr zirconates and might reflect a difficulty in quantifying the occupancy when protons are mobile at the measurement temperatures. Given this difficulty, Figure S1 also includes plots of CCEs measured in this work vs. reported absolute proton concentrations [1] at each isotherm in four of the compositions studied under a pH₂O of \sim 0.02 in other work, showing no clear relationship. In summary, we expect moderate to high proton concentrations relative to the acceptor concentration in the conditions of this study, small proton concentration changes resulting in linear chemical strain behavior, and no obvious relationship of CCE to absolute proton concentration.

5. Summary and Conclusions

Isothermal hydration coefficients of chemical expansion are measured for the SrCe_{0.9}. $_xZr_xY_{0.1}O_3$ solid solution using dilatometry for chemical strains and TGA for stoichiometry changes, and these results are compared with prior isothermal measurements on the BaCe_{0.9}. $_xZr_xY_{0.1}O_3$ solid solution to determine the consistency of factors that correlate to hydration CCE trends. High temperature *in-situ* neutron diffraction is applied to determine atomic positions that inform how defects are accommodated in each lattice. We find that $SrZr_{0.9}Y_{0.1}O_3$ undergoes a significant decrease in B-O-B bond angle after hydration, while $SrCe_{0.9}Y_{0.1}O_3$ and $BaZr_{0.9}Y_{0.1}O_3$ do not demonstrate noticeable bond angle changes. More significant changes in bond angles during hydration likely help to accommodate defect strains in the lattice via subtle deformations, rather than volumetric expansion. The ability of a composition to accommodate defect strains in this

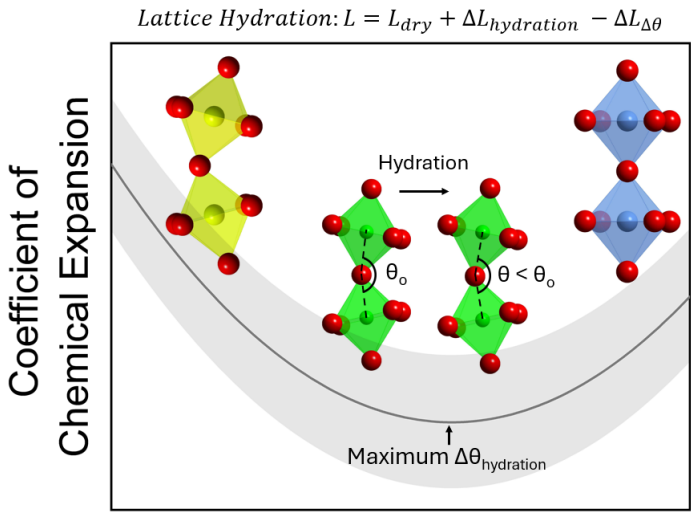
manner may correlate to the low hydration CCEs observed in the intermediate tolerance factor range t = 0.93 - 0.95 for both $SrCe_{0.9-x}Zr_xY_{0.1}O_3$ and $BaCe_{0.9-x}Zr_xY_{0.1}O_3$ solid solutions. The potential influence of crystal symmetry and lattice distortions, unit cell size, oxygen vacancy size, strain anisotropy, and microstructure on CCE are all discussed. Notably, chemical strain anisotropy increases as tolerance factor decreases, but the hydration CCE does not follow the same trend. Variability of chemical strain magnitudes is observed in some replicate samples, attributed to microstructure differences, indicating that grain sizes and pore distribution should be further studied to determine their effects on hydration CCE.

Acknowledgments

This work was supported financially by a NSF CAREER grant to NHP (DMR-1945482). The use of facilities and instrumentation was supported by NSF through the University of Illinois Materials Research Science and Engineering Center (DMR-2309037) for the Bruker D8 Advance XRD measurements and by the Materials Research Laboratory Central Research Facilities, University of Illinois for SEM work with the JEOL JSM-7000F Analytical SEM. This research used resources at the Spallation Neutron Source, a DOE Office of Science User Facility operated by the Oak Ridge National Laboratory. We acknowledge the technical assistance provided by Melanie Kirkham during the POWGEN experiment.

Supporting Information: Example refinement outcomes from neutron diffraction when H site occupancy is not constrained, showing also the cation site fractions determined from X-ray fluorescence (Table 1); comparison of measured hydration CCEs with reported absolute proton concentrations from literature showing no relationship (Figure S1).

Table of Contents Figure



tolerance factor

References

- [1] K. D. Kreuer, "Proton-Conducting Oxides," *Annu Rev Mater Res*, vol. 33, pp. 333–359, 2003, doi: 10.1146/annurev.matsci.33.022802.091825.
- [2] H. Iwahara, Y. Asakura, K. Katahira, and M. Tanaka, "Prospect of hydrogen technology using proton-conducting ceramics," *Solid State Ion*, vol. 168, no. 3–4, pp. 299–310, 2004, doi: 10.1016/j.ssi.2003.03.001.
- [3] A. Kushima and B. Yildiz, "Oxygen ion diffusivity in strained yttria stabilized zirconia: Where is the fastest strain?," *J Mater Chem*, 2010, doi: 10.1039/c000259c.
- [4] V. V. Sereda, D. S. Tsvetkov, D. A. Malyshkin, I. L. Ivanov, A. L. Sednev-Lugovets, and A. Y. Zuev, "Hydration-induced chemical expansion of BaCa(1+y)/3Nb(2-y)/3O3-δ·xH2O (BCN) and other proton-conducting perovskite oxides," *Solid State Ion*, vol. 358, p. 115516, 2020, doi: 10.1016/j.ssi.2020.115516.
- [5] T. Chen *et al.*, "Toward Durable Protonic Ceramic Cells: Hydration-Induced Chemical Expansion Correlates with Symmetry in the Y-Doped BaZrO3–BaCeO3 Solid Solution," *The Journal of Physical Chemistry C*, vol. 125, no. 47, pp. 26216–26228, Dec. 2021, doi: 10.1021/ACS.JPCC.1C08334.
- [6] A. K. E. E. Andersson, S. M. Selbach, C. S. Knee, and T. Grande, "Chemical expansion due to hydration of proton-conducting perovskite oxide ceramics," *Journal of the American Ceramic Society*, vol. 97, no. 8, pp. 2654–2661, Aug. 2014, doi: 10.1111/jace.12990.

- [7] T. S. Bjørheim, A. Løken, and R. Haugsrud, "On the relationship between chemical expansion and hydration thermodynamics of proton conducting perovskites," *J Mater Chem A Mater*, vol. 4, no. 16, pp. 5917–5924, Apr. 2016, doi: 10.1039/c5ta10090a.
- [8] F. G. Kinyanjui, S. T. Norberg, I. Ahmed, S. G. Eriksson, and S. Hull, "In-situ conductivity and hydration studies of proton conductors using neutron powder diffraction," *Solid State Ion*, vol. 225, pp. 312–316, 2012, doi: 10.1016/j.ssi.2012.05.018.
- [9] K. Leonard, Y. S. Lee, Y. Okuyama, K. Miyazaki, and H. Matsumoto, "Influence of dopant levels on the hydration properties of SZCY and BZCY proton conducting ceramics for hydrogen production," *Int J Hydrogen Energy*, vol. 42, no. 7, pp. 3926–3937, 2017, doi: 10.1016/j.ijhydene.2016.10.120.
- [10] J. Hermet, F. Bottin, G. Dezanneau, and G. Geneste, "Thermodynamics of hydration and oxidation in the proton conductor Gd-doped barium cerate from density functional theory calculations," *Phys Rev B Condens Matter Mater Phys*, vol. 85, no. 20, p. 205137, 2012, doi: 10.1103/PhysRevB.85.205137.
- [11] D. Poetzsch, R. Merkle, and J. Maier, "Proton uptake in the H+-SOFC cathode material Ba0.5Sr0.5Fe0.8Zn0.2O3-d: transition from hydration to hydrogenation with increasing oxygen partial pressure," *Faraday Discuss*, vol. 182, pp. 129–143, 2015, doi: 10.1039/c5fd00013k.
- [12] J. S. Park, J. H. Lee, H. W. Lee, and B. K. Kim, "Low temperature sintering of BaZrO3-based proton conductors for intermediate temperature solid oxide fuel cells," *Solid State Ion*, vol. 181, no. 3–4, pp. 163–167, 2010, doi: 10.1016/j.ssi.2009.06.015.
- [13] D. S. Yun *et al.*, "Structural and electrochemical properties of dense yttria-doped barium zirconate prepared by solid-state reactive sintering," *Energies (Basel)*, vol. 11, no. 11, p. 3083, 2018, doi: 10.3390/en1113083.
- [14] M. Shirpour, R. Merkle, C. T. Lin, and J. Maier, "Nonlinear electrical grain boundary properties in proton conducting Y-BaZrO3 supporting the space charge depletion model," *Physical Chemistry Chemical Physics*, vol. 14, no. 2, pp. 730–740, 2012, doi: 10.1039/c1cp22487e.
- [15] A. Lacz, K. Grzesik, and P. Pasierb, "Electrical properties of BaCeO3-based composite protonic conductors," *J Power Sources*, vol. 279, pp. 80–87, 2015, doi: 10.1016/j.jpowsour.2014.12.065.
- [16] T. Hibino and H. Iwahara, "CO2 sensors using BaCeO3-based ceramics," *Sens Actuators B Chem*, vol. 13, no. 1–3, pp. 483–485, 1993, doi: 10.1016/0925-4005(93)85433-B.
- [17] J. Wallis *et al.*, "Structural and electrical properties of BaZr0.7Ce0.2Y0.1O3–δ proton conducting ceramic fabricated by spark plasma sintering," *Solid State Ion*, vol. 345, p. 115118, 2020, doi: 10.1016/j.ssi.2019.115118.
- [18] J. S. Park, J. H. Lee, H. W. Lee, and B. K. Kim, "Low temperature sintering of BaZrO3-based proton conductors for intermediate temperature solid oxide fuel cells," *Solid State Ion*, vol. 181, no. 3–4, pp. 163–167, 2010, doi: 10.1016/j.ssi.2009.06.015.
- [19] D. S. Yun *et al.*, "Structural and electrochemical properties of dense yttria-doped barium zirconate prepared by solid-state reactive sintering," *Energies (Basel)*, vol. 11, no. 11, p. 3083, 2018, doi: 10.3390/en11113083.

- [20] M. Shirpour, R. Merkle, C. T. Lin, and J. Maier, "Nonlinear electrical grain boundary properties in proton conducting Y-BaZrO3 supporting the space charge depletion model," *Physical Chemistry Chemical Physics*, vol. 14, no. 2, pp. 730–740, 2012, doi: 10.1039/c1cp22487e.
- [21] A. Lacz, K. Grzesik, and P. Pasierb, "Electrical properties of BaCeO3-based composite protonic conductors," *J Power Sources*, vol. 279, pp. 80–87, 2015, doi: 10.1016/j.jpowsour.2014.12.065.
- [22] T. Hibino and H. Iwahara, "CO2 sensors using BaCeO3-based ceramics," *Sens Actuators B Chem*, vol. 13, no. 1–3, pp. 483–485, 1993, doi: 10.1016/0925-4005(93)85433-B.
- [23] A. Løken, S. Ricote, and S. Wachowski, "Thermal and chemical expansion in proton ceramic electrolytes and compatible electrodes," *Crystals (Basel)*, vol. 8, no. 9, p. 365, Sep. 2018, doi: 10.3390/cryst8090365.
- [24] E. Jedvik, A. Lindman, M. P. Benediktsson, and G. Wahnström, "Size and shape of oxygen vacancies and protons in acceptor-doped barium zirconate," *Solid State Ion*, vol. 275, pp. 2–8, Jul. 2015, doi: 10.1016/j.ssi.2015.02.017.
- [25] R. D. Shannon, "Revised effective ionic radii and systematic studies of interatomic distances in halides and chalcogenides," *Acta Crystallographica Section A*, vol. 32, no. 5, pp. 751–767, 1976, doi: 10.1107/S0567739476001551.
- [26] M. Kirkham, L. Heroux, M. Ruiz-Rodriguez, and A. Huq, "AGES: Automated Gas Environment System for in situ neutron powder diffraction," *Review of Scientific Instruments*, vol. 89, no. 9, p. 92904, Sep. 2018, doi: 10.1063/1.5031432/16758752/092904 1 ACCEPTED MANUSCRIPT.PDF.
- [27] H. Wang, C. Tablet, W. Yang, and J. Caro, "In situ high temperature X-ray diffraction studies of mixed ionic and electronic conducting perovskite-type membranes," *Mater Lett*, vol. 59, no. 28, pp. 3750–3755, Dec. 2005, doi: 10.1016/J.MATLET.2005.06.067.
- [28] M. Bahout *et al.*, "Stability of NdBaCo2 $-xMnxO5+\delta$ (x=0,0.5) layered perovskites under humid conditions investigated by high-temperature in situ neutron powder diffraction," *J Mater Chem A Mater*, vol. 3, no. 30, pp. 15420-15431, Jul. 2015, doi: 10.1039/C5TA02776D.
- [29] B. H. Toby and R. B. Von Dreele, "GSAS-II: the genesis of a modern open-source all purpose crystallography software package," *J Appl Crystallogr*, vol. 46, no. 2, pp. 544–549, Apr. 2013, doi: 10.1107/S0021889813003531.
- [30] K. Momma and F. Izumi, "VESTA 3 for three-dimensional visualization of crystal, volumetric and morphology data," *urn:issn:0021-8898*, vol. 44, no. 6, pp. 1272–1276, Oct. 2011, doi: 10.1107/S0021889811038970.
- [31] T. Chen *et al.*, "Toward Durable Protonic Ceramic Cells: Hydration-Induced Chemical Expansion Correlates with Symmetry in the Y-Doped BaZrO3–BaCeO3 Solid Solution," *The Journal of Physical Chemistry C*, vol. 125, no. 47, pp. 26216–26228, Dec. 2021, doi: 10.1021/ACS.JPCC.1C08334.
- [32] T. Fujisaki, A. T. Staykov, Y. Jing, K. Leonard, N. R. Aluru, and H. Matsumoto, "Understanding the effect of Ce and Zr on chemical expansion in yttrium doped strontium cerate and zirconate by high temperature X-ray analysis and density functional theory," *Solid State Ion*, vol. 333, pp. 1–8, 2019, doi: 10.1016/j.ssi.2019.01.009.

- [33] A. Cammarata and J. M. Rondinelli, "Covalent dependence of octahedral rotations in orthorhombic perovskite oxides," *Journal of Chemical Physics*, vol. 141, p. 114704, 2014, doi: 10.1063/1.4895967.
- [34] A. M. Glazer and IUCr, "The classification of tilted octahedra in perovskites," *urn:issn:0567-7408*, vol. 28, no. 11, pp. 3384–3392, Nov. 1972, doi: 10.1107/S0567740872007976.
- [35] T. Fujisaki, K. Hinata, F. Iguchi, N. Dimov, A. T. Staykov, and H. Matsumoto, "Understanding the difference in bulk modulus between Y-doped SrCeO 3 and Y-doped SrZrO 3 by ultrasonic transmission method and density functional theory," 2022, doi: 10.1016/j.mtla.2022.101616.
- [36] C. Chatzichristodoulou, P. Norby, P. V. Hendriksen, and M. B. Mogensen, "Size of oxide vacancies in fluorite and perovskite structured oxides," *J Electroceram*, 2015, doi: 10.1007/s10832-014-9916-2.
- [37] K. Zhang, Q. Meng, X. Zhang, Z. Qu, S. Jing, and R. He, "Roles of solid loading in stereolithography additive manufacturing of ZrO 2 ceramic," *Int J Refract Metals Hard Mater*, vol. 99, p. 105604, 2021, doi: 10.1016/j.ijrmhm.2021.105604.
- [38] S. Yang, Y. Lu, Q. Wang, C. Sun, X. Ye, and Z. Wen, "Effects of porous support microstructure enabled by the carbon microsphere pore former on the performance of proton-conducting reversible solid oxide cells," 2018, doi: 10.1016/j.ijhydene.2018.09.011.
- [39] D. Kuscer, I. Bantan, M. Hrovat, and B. Malič, "The microstructure, coefficient of thermal expansion and flexural strength of cordierite ceramics prepared from alumina with different particle sizes," *J Eur Ceram Soc*, vol. 37, pp. 739–746, 2017, doi: 10.1016/j.jeurceramsoc.2016.08.032.
- [40] M. Aghajanian, C. Emmons, S. Rummel, P. Barber, C. Robb, and D. Hibbard, "Effect of grain size on microstructure, properties, and surface roughness of reaction bonded SiC ceramics," *Material Technologies and Applications to Optics, Structures, Components, and Sub-Systems*, vol. 8837, no. September 2013, p. 88370J, 2013, doi: 10.1117/12.2024308.
- [41] D.-M. Liu and J. J. Brown, "Thermal expansion of porous (Ca, 1-x, Mgx)Zr4(P04)6 ceramics," *Materials ChemrStry and Physics*, vol. 33, p. 43, 1993.
- [42] T. H. Nielsen and M. H. Leipold, "Thermal Expansion in Air of Ceramic Oxides to 2200°C", doi: 10.1111/j.1151-2916.1963.tb11756.x.